Vacuum 212 (2023) 112045

Contents lists available at ScienceDirect

Vacuum

journal homepage: www.elsevier.com/locate/vacuum

Laser-induced electron dynamics and surface modification in ruthenium thin films

Fedor Akhmetov [a,*], Igor Milov [a], Sergey Semin [b], Fabio Formisano [b], Nikita Medvedev [c,d], Jacobus M. Sturm [a], Vasily V. Zhakhovsky [e], Igor A. Makhotkin [a], Alexey Kimel [b], Marcelo Ackermann [a]

[a] Industrial Focus Group XUV Optics, MESA+ Institute for Nanotechnology, University of Twente, Drienerlolaan 5, Enschede, 7522 NB, The Netherlands
[b] Institute for Molecules and Materials, Radboud University Nijmegen, Heyendaalseweg 135, Nijmegen, 6525 AJ, The Netherlands
[c] Institute of Physics, Czech Academy of Sciences, Na Slovance 1999/2, Prague 8, 182 21, Czech Republic
[d] Institute of Plasma Physics, Czech Academy of Sciences, Za Slovankou 3, Prague 8, 182 00, Czech Republic
[e] Joint Institute for High Temperatures, RAS, Izhorskaya St. 13/2, Moscow, 125412, Russia

ARTICLE INFO

Keywords:
Femtosecond laser damage
Thin films
Ruthenium
Two-temperature molecular dynamics
Fermi smearing
Pump-probe thermoreflectance

ABSTRACT

We performed the experimental and theoretical study of the heating and damaging of ruthenium thin films induced by femtosecond laser irradiation. We present the results of an optical pump-probe thermoreflectance experiment with rotating sample allowing to significantly reduce heat accumulation in irradiated spot. We show the evolution of surface morphology from growth of a heat-induced oxide layer at low and intermediate laser fluences to cracking and grooving at high fluences. Theoretical analysis of thermoreflectance in our pump-probe experiment allows us to relate behavior of hot electrons in ruthenium to the Fermi smearing mechanism. This conclusion invites more research on Fermi smearing of transition metals. The analysis of heating is performed with the two-temperature modeling and molecular dynamics simulation, results of which demonstrate that the calculated single-shot melting threshold is higher than experimental damage threshold. We suggest that the onset of Ru film damage is caused by the heat-induced stresses that lead to cracking of the Ru film. Such damage accumulates during repetitive exposure to light.

1. Introduction

Ultrashort lasers have become versatile tools for the manipulation of material properties at the nanoscale. The unique ability of such lasers to deliver an enormous amount of energy into a sample on a femtosecond timescale creates extreme strongly non-equilibrium states which upon relaxation lead to altered material properties. Ultrashort lasers are used for surface nanostructuring [1] and nanofabrication [2–4], as well as for reversible switching of material structure between crystal and amorphous phases for applications in data storage [5]. Alternatively to these high-intensity laser applications, ultrashort lasers with relatively low intensity are used in various metrology and probing techniques [6–8]. In this context, contrary to the previous examples, laser-induced damage must be avoided. In both scenarios of desired and undesired material modifications, precise control of the output of laser–matter interaction is crucial, and can only be achieved with a deep understanding of the fundamental physical processes involved. This work aims at such understanding on an example of ruthenium (Ru) thin films exposed to optical femtosecond laser pulses.

Ru and Ru oxides are indispensable materials for various catalysis applications [9,10]. Controlling the surface properties of Ru such as oxidation state, as well as the shape and structure of Ru nanocrystals, provides additional efficient functionalities [11]. Ultrathin films of Ru are used as protective capping layers in extreme ultraviolet optics, due to high transmissivity in EUV range and low surface oxidation [12]. Ru is also considered as a high Z material for grazing incidence hard X-ray optics [13].

In our previous studies, we focused on severe damage of Ru thin films at high vacuum conditions in single- [14–16] and multi-shot regimes [17], as well as on long-term exposure of Ru at fluences significantly below the single-shot ablation threshold [18]. Such sub-threshold investigation of material degradation is challenging since the processes involved are elusive to be detected *post mortem*. Dynamical data must be collected to provide insights into how laser-induced evolution of Ru results in the final damage. Therefore, in this work, we continue investigating Ru interaction with ultrashort laser pulses in an all-optical pump-probe scheme with rotating samples to reduce

* Corresponding author.
E-mail address: f.akhmetov@utwente.nl (F. Akhmetov).

https://doi.org/10.1016/j.vacuum.2023.112045
Received 17 October 2022; Received in revised form 21 March 2023; Accepted 24 March 2023
Available online 27 March 2023

heat accumulation effects. The analysis of measured in pump-probe experiment thermoreflectance data aimed to find a connection between optical response and light-induced damage of a film.

The character of damage may depend on certain environmental conditions. For example, the single- and multi-pulse damage thresholds of optical coatings may alter depending whether the experiments are carried out at vacuum or ambient conditions [19]. The presence of oxygen in the environment enhances the darkening of a metal surface during the ultrafast laser ablation [20]. The influence of environment on surface nanopattering does not demonstrate any systematic behavior. In some experimental configurations, the pressure of gas plays a major role whereas the chemical altering of surface has minor impact [21]. In others, the chemical composition of gas determines the morphology of nanostructures [22].

We performed present experiment under ambient conditions. After the irradiation, Ru surfaces are examined with various surface-sensitive characterization techniques, namely Atomic Force Microscopy (AFM), Auger- and X-ray photo-electron spectroscopies (AES and XPS) and Scanning Electron Microscopy (SEM). Determination of Ru thin film damage threshold was based on a SEM analysis of exposed samples. The analysis of pristine and irradiated surface revealed only a minor effect of environment on detected damage. This indicates that at given irradiation parameters similar character of damage can be expected under vacuum conditions.

To interpret pump-probe data we perform theoretical analysis of Ru optical response to ultrashort laser irradiation. When an ultrafast laser pulse illuminates a metallic target, its energy is absorbed by the conduction band electrons, which leads to the evolution of initially equilibrium electron distribution to a non-equilibrium one. It is often assumed that the thermalization of an electron gas to an equilibrium Fermi distribution occurs on a timescale of ~100 fs, which is comparable to our pulse duration [23–26]. Thus, it is convenient to consider the probed optical response of a metallic target in terms of the electron temperature T_e elevated with respect to the lattice one T_l. However, a reliable model for T_e-dependent optical constants is required for direct analysis of optical pump-probe experiments. The widely used Drude model is limited in applicability to the case of simple metals [27]. In the case of noble metals, the optical response can be successfully described by Fermi smearing mechanism, assuming that change of reflection signal is proportional to the derivative of the Fermi distribution with respect to the electron temperature [28–30].

In contrast, in a transition metal with a complex band structure such as Ru, the optical constants are formed by a sum of *inter*- and *intraband* contributions within a combined d-s/p conduction band and to date could not be reasonably approximated with a simple analytical model. Instead, T_e-dependence may be extracted from first-principles simulations of the complex dielectric function of a material in, e.g., random-phase approximation (RPA) [31–34]. However, such simulations are computationally heavy.

We test to what extent a simple Fermi smearing analysis can be applied to Ru. We also model the absorption of the laser energy by the electrons and coupling of electrons to the lattice with the two-temperature model (TTM) and with a combination of the TTM with classical molecular dynamics. The calculated single-shot melting threshold is compared with the experimental surface modification observations.

2. Experimental setup

For the pump-probe thermoreflectance experiments, we employed pump-probe set-up based on ultrafast 1 kHz repetition rate Ti:Sapphire laser, Fig. 1. The experiment was carried out under atmospheric conditions. The angles of incidence (AOI) were set close to normal (~5 ± 2° and ~8±2° off-sample normal for pump and probe pulses, respectively). The beam profile was characterized by a knife-edge method along the horizontal direction. Additional *post mortem* analysis of Ru ablation craters revealed an ellipticity of a Gaussian profile which is not associated with a small off-normal AOI only. The value of the semi-major axis was ~115 μm (@ $1/e^2$) whereas the value of the semi-minor axis was 1.4 times smaller. The peak incident fluence was calculated as follows:

$$F = \frac{2E_{pulse}}{\pi w_x w_y} \quad (1)$$

Here E_{pulse} is an energy value of pump pulse, w_x and w_y are values of semi-major and semi-minor axes of ellipse, respectively. The sample was positioned slightly before the focal spot to avoid air ionization and consequent aberration of the beam quality at the sample. To continuously control the laser fluence we used an attenuator consisting of a half-wave plate and a polarizer located in the pump path. We characterized the laser pulse duration by placing an autocorrelator just before the sample with typical measured values to be ~85 fs (FWHM). P- and s-polarizations with respect to the optical bench were used for the pump and the probe pulse, respectively.

As a studied material, we used ruthenium (Ru) polycrystalline thin metal film. The Ru films of various thickness between 17 and 125 nm were deposited by magnetron sputtering on top of (100) single-crystal Si wafers with 3-inch diameter. Ru thickness was measured using X-ray reflectometry. To reduce the effect of heat accumulation, samples were mounted on a rotational stage. The rotational frequency was set to $\omega = 90$ Hz. Such a scheme ensured an effective reduction of the repetition rate, without changes of the laser source. However, after several rotations laser pulses start hitting previously exposed surface, therefore accumulation of irreversible changes induced by pump pulses is expected at high pump fluences. For each sample we measured transient thermoreflectance change induced by pump pulses of various fluences. For each fluence value a different position on a sample was measured. For every sample, the measurements were carried out at distances in the range of 17–32 mm from a sample center. Since the position variation was small compared to the radius at which the set of measurements was performed, a slightly different level of accumulation of irreversible changes for different fluences within each sample can be neglected.

Before the actual measurement of thermoreflectance curve, several pump and probe pulses arrive to the sample surface at negative delays between the pump and the probe resulting in a weak signal. We have a pronounced step in this signal at negative delays from −20 to 0 ps (see Fig. 2(a)). We explain it by a partial split of the probe signal in the beamsplitter leading to a delay between the main fraction of probe and a small trailing probe. The latter overlaps with the retarding pump pulse and delivers a small signal to the photo-detector. Analyzing thermoreflectance data, we aligned the signal to the values taken from delays $t < -20$ ps.

3. Experimental results

3.1. Fluence-dependent transient thermoreflectance

A set of pump-probe transient thermoreflectance data for a 37 nm thick Ru film is shown in Fig. 2(a). It demonstrates that in all measured curves the reflected probe intensity sharply increases during the first few ps resulting in a pronounced peak followed by slow decay. The very sharp increase at <1 ps timescales is primarily associated with the increase of the electron temperature induced by the absorbed pump pulse. At ~1–3 ps timescale, a slower signal increase can be attributed to the coupling of the electrons to the lattice and thereby induced lattice heating. A slow decay over tens of picoseconds corresponds to heat diffusion from the surface region deeper into the sample [35]. This is confirmed by the TTM simulations of the surface electron and lattice temperatures shown in Fig. 2(b).

At high pump pulse fluences above ~50 mJ/cm^2 we observe qualitatively different behavior of $\Delta R/R_0$ signal at $\Delta t > 20$ ps time delay

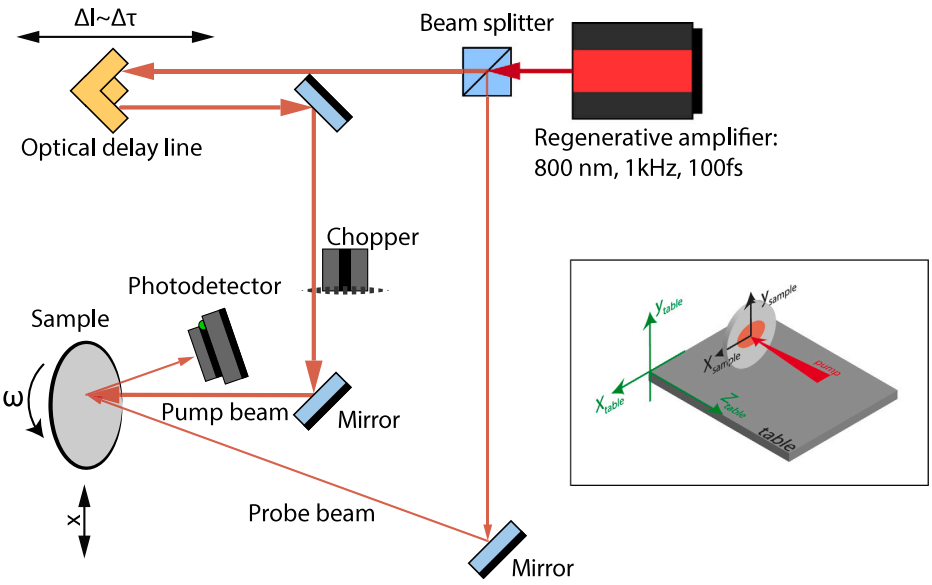

Fig. 1. Scheme of experimental set-up used for optical pump-probe thermoreflectance measurements. The laser beam coming out of regenerative amplifier (Spitfire), which generates the near transform-limited 100 fs FWHM pulses with 800 nm wavelength ($\hbar\omega = 1.55$ eV) and 1 kHz repetition rate. Laser beam is split into a high-intensity pump and a low-intensity probe pulses. The pump pulse is chopped to a 500 Hz repetition rate. The probe pulse at 1 kHz arrives to the sample with a time delay controlled with an optical delay line to measure the reflection change induced by the pump pulse. Inset: configuration of polarization of incident beams and convention on axes.

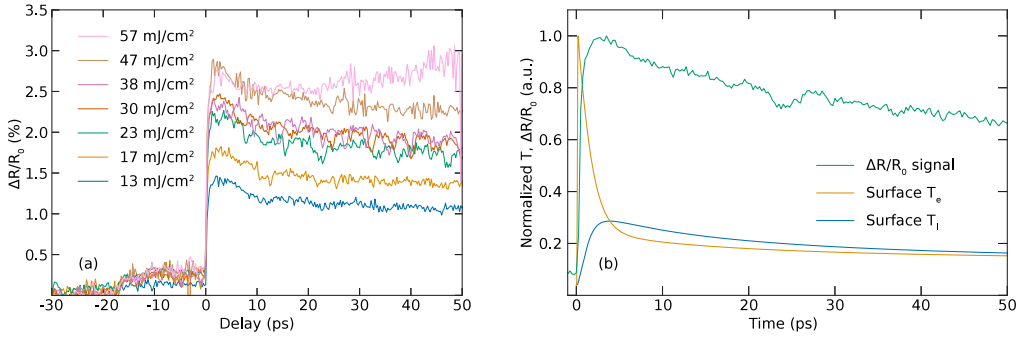

Fig. 2. (a) Transient changes of reflectance of a 37 nm Ru film measured for various incident fluences. (b) Normalized pump-probe thermoreflectance signal (green) compared with normalized profiles of electron (orange) and lattice (blue) temperatures.

compared to lower fluences. We see the change of trend from a slow decay to an increase. For every thickness, we were able to extract the time when the signal starts to increase by calculating the time derivative of a signal using a regularization algorithm for noisy signals [36]. We determined the time and fluence values when a derivative of a signal changes its sign from negative to positive, and report them in Table 1. For 17 nm Ru film, we could not extract any values, because the pump-probe curves exhibit strong oscillations for high fluence values. For 125 nm Ru film, we did not observe an increase of the signal within the fluence and time delay ranges considered, and thus put the highest measured fluence into the table. We use these data later in Section 4.3 when discussing the thickness-dependent damage threshold in Ru.

The measured data in Fig. 2(b) show that the peak thermoreflectance change reached at ~3 ps for each curve increases with the fluence and saturates at a certain fluence value. Similar sets of pump-probe thermoreflectance curves were obtained for various thicknesses of Ru films. The overview of measured data for all film thicknesses is reported in the supplementary materials.

In Fig. 3 we provide the peak values of $\Delta R/R_0$ as a function of the pump fluence for three different thicknesses of Ru corresponding to three absorption regimes (see more details in Fig. 4). The optical penetration depth in Ru for 800 nm light is 16 nm. Therefore, for 17 nm film, multiple reflections of absorbed light at a Ru–Si and Ru–air interfaces change the absorption profile considerably compared to the Lambert–Beer law. For 37 nm, deviations from the Lambert–Beer profile are visible but not dramatic, whereas 125 nm film optically behaves like a bulk material, see Fig. 4. We see that with increasing fluence the peak of reflectance linearly increases and saturates at a particular value for each Ru thickness.

In the case of 37 nm Ru, we see a jump in the peak values of thermoreflectance around 45 mJ/cm^2. The further analysis does not reveal any sharp changes at this fluence, and such a jump is not present in the data obtained from other samples, the peak reflectance changes continuously. Therefore, we consider it to be a measurement artefact. In the case of 125 nm Ru, we observe a drop of reflectance peak at the

Table 1
Measured fluence and time delay values related to change of signal trend from slow decay to sharp increase at high fluence.

Thickness, nm	Incident fluence, mJ/cm^2	Absorbed fluence, mJ/cm^2	Delay, ps
17	–	–	–
30	51.2 ± 3.8	14.1 ± 1.0	25.5
37	54.6 ± 4.0	16.7 ± 1.2	36.0
50	60.9 ± 4.5	21.7 ± 1.6	21.5
75	67.2 ± 4.9	25.9 ± 1.9	21.8
125	77.0 ± 5.7	29.9 ± 2.2	–

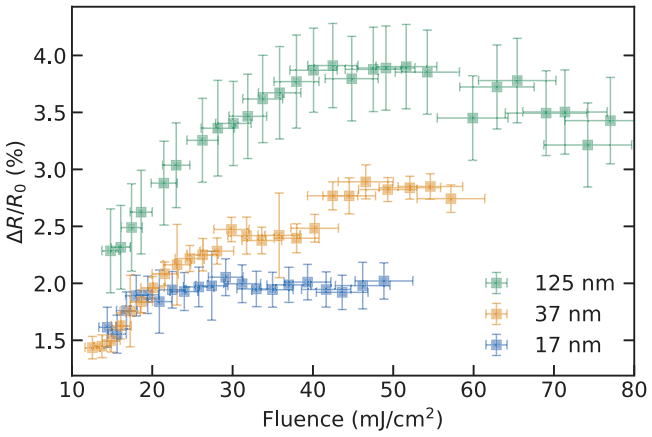

Fig. 3. Peak values of thermoreflectance change as a function of pump fluence for 17 nm, 37 nm, and 125 nm Ru films.

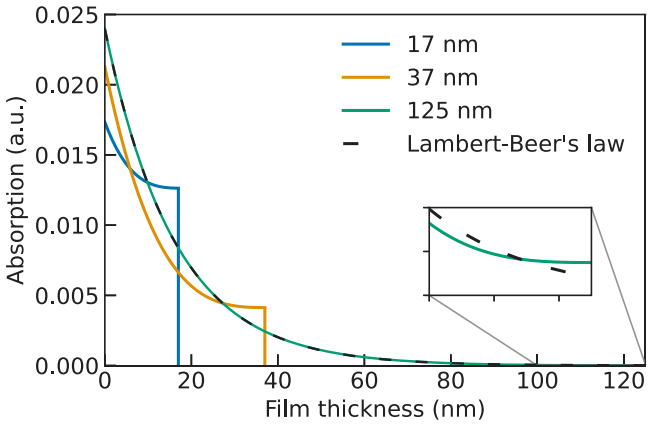

Fig. 4. Absorbed energy density profiles for Ru films of 17, 37, and 125 nm thicknesses on Si substrates calculated with the transfer-matrix approach [37]. Inset: deviation of transfer-matrix from Lambert–Beer profile at Ru–Si interface.

highest fluences. We also detected a similar drop at another thickness, 75 nm. We attribute these drops to strong accumulated damage of a film at high fluences. This is confirmed by SEM observations presented in Section 3.2, where we observed strong damage of sample surfaces at high fluences.

3.2. Analysis of the surface morphology

Since the experiment is carried out with rotation of samples, having rotation frequency and laser repetition rate unsynchronized, the pump laser generates not individual spots, but almost continuous lines. Every line corresponds to a particular laser fluence, so we can easily trace possible morphology changes caused by the pump using *post mortem* SEM analysis.

In Fig. 5 we show SEM images of a 37 nm thick Ru film surface after laser exposure. Fig. 5(a) shows the overview SEM image of exposed lines. The line 1 corresponds to the highest peak fluence of 57 mJ/cm^2, the last visible line (line 10) corresponds to the peak fluence of 36 mJ/cm^2. Note that before actual damage of the surface, several lines look darker compared to unexposed area. In Fig. 5(b) we show the magnified view of line 4 (peak fluence is 49 mJ/cm^2). At those irradiation conditions, SEM was not able to resolve any morphological changes of the surface. Starting from line 3 we see a clear indication of damage: the film is covered with cracks (Fig. 5(c)). Further increase of the peak fluence leads to severe damage of the surface having a shape of periodic grooves, see Fig. 5(d).

To investigate in more details the onset of damage, we also performed cross-sectional SEM scans of cracked area, see Fig. 6. They revealed that the cracks are formed over the entire film depth. We will discuss possible mechanisms of crack formation below in Section 4.3.

For the analysis of a dark region on line 4, we performed an additional combination of Auger electron spectroscopy (AES), X-ray photoelectron spectroscopy (XPS), and atomic force microscopy (AFM) characterization techniques. AES indicated ~2 times increase of oxygen concentration on the dark regions, compared to the reference area outside the exposure zones. A more detailed measurement of the oxide thickness done with angle-resolved XPS indicated only 0.4 nm growth of the oxide layer above the thickness of a native oxide of 0.8 nm. Such a small increase of oxygen content after irradiation at relatively high incident fluence means that the oxidation is not responsible for film damage. Under given irradiation parameters, one can expect similar behavior at vacuum conditions.

The AFM indicated ~1.5 times increased RMS roughness in these exposed areas from 0.187 nm to 0.280 nm. It is unlikely that such small structural changes can explain the formation of dark lines on the SEM image. We can assume possible light-induced carbon growth that could explain such darkening. However, the growth of small amounts of C on Ru cannot be reliably quantified by AES and XPS, because carbon and ruthenium emission spectra overlap on Auger electron/X-ray photoemission spectra. The XPS spectra in the exposed spot showed an increase of the intensity at the energy of the Ru3d$_{3/2}$ peak relative to the Ru3d$_{5/2}$ intensity (compared to outside the exposed area). This is a qualitative indication of increased carbon content, but the difference compared to the unexposed area is too small for a reliable quantification by peak fitting. Detailed description of XPS analysis is provided in Appendix A.

We can claim that the darkening of an irradiated path is a result of heat-induced surface chemistry. We found that the darkening is a result of a minor increase of the oxide thickness as well as slight carbonization. However, we could not resolve the exact stoichiometry of the compound since the carbon signal was too weak to quantify.

4. Theoretical analysis

4.1. Two-temperature modeling

For the analysis of laser-induced ultrafast heating and melting of Ru thin films, we applied the two-temperature model (TTM) [38]. The TTM equations that govern heat dynamics of electron and lattice subsystems are:

$$\begin{cases} C_e(T_e)\frac{\partial T_e}{\partial t} = \frac{\partial}{\partial z}\left(k_e(T_e,T_l)\frac{\partial T_e}{\partial z}\right) - G(T_e,T_l)(T_e - T_l) + S(t,z), \\ \left(C_l(T_l) + H_m\delta(T_l - T_m)\right)\frac{\partial T_l}{\partial t} = G(T_e,T_l)(T_e - T_l) \end{cases} \quad (2)$$

Here T, C and k are the temperature, heat capacity and thermal conductivity of Ru electrons (subscript e) and lattice (subscript l), respectively; G is the temperature-dependent electron–phonon coupling factor, and S is the heat source representing a laser pulse. Lattice thermal conductivity is considered to be negligible compared to the electron one. The electron heat capacity and electron–phonon coupling were taken from XTANT simulations based on the non-adiabatic tight-binding molecular dynamics approach [39]. The electron thermal conductivity $k_e(T_e,T_l)$ was taken from *ab initio* calculations [40], and that is the most accurate data available to the best of our knowledge.

To account for solid–liquid phase transition at the melting temperature T_m, we used an effective lattice heat capacity containing a delta-function term corresponding to the latent heat of fusion H_m, as was initially proposed in [41] for ns-laser heating, and latter extended in [42] to TTM approach and fs pulses. The melting threshold was considered to be reached when at least one computational cell came to a liquid state ($T_l > T_m$).

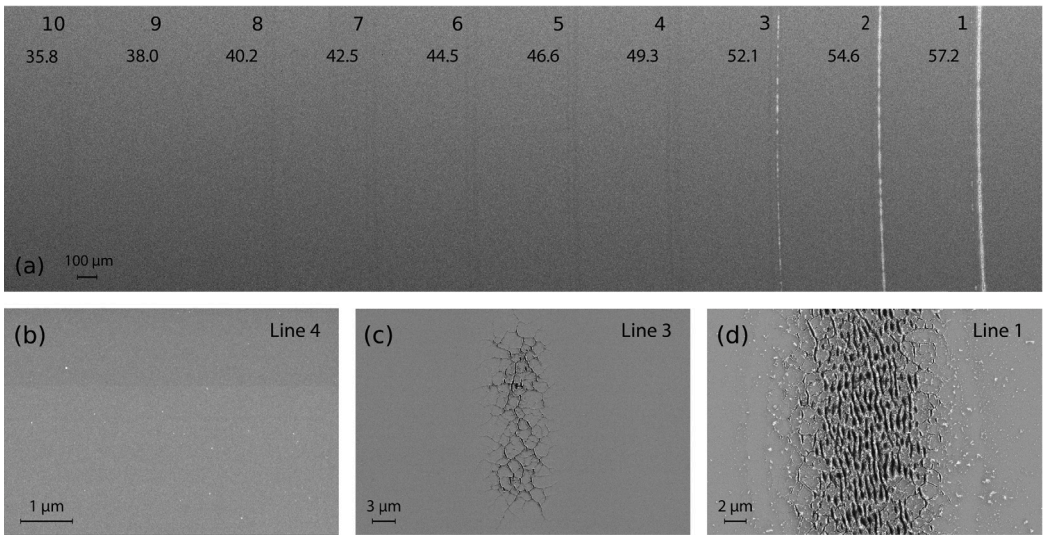

Fig. 5. (a) SEM image of a 37 nm thick Ru surface after laser irradiation. Numbered lines correspond to irradiation conditions ranging from the regime of intermediate fluences (lines 10–4, darkening along irradiation path) to high (lines 3–1, the surface is damaged), and the values below the line numbers are pulse fluences in mJ/cm^2. (b) Zoomed-in SEM image of line 4, no surface damage is present. (c) The same for line 3. The line consists of separate spots of cracks along the irradiation path. (d) The same for line 1. Damage morphology is represented by continuous grooves along the irradiation path.

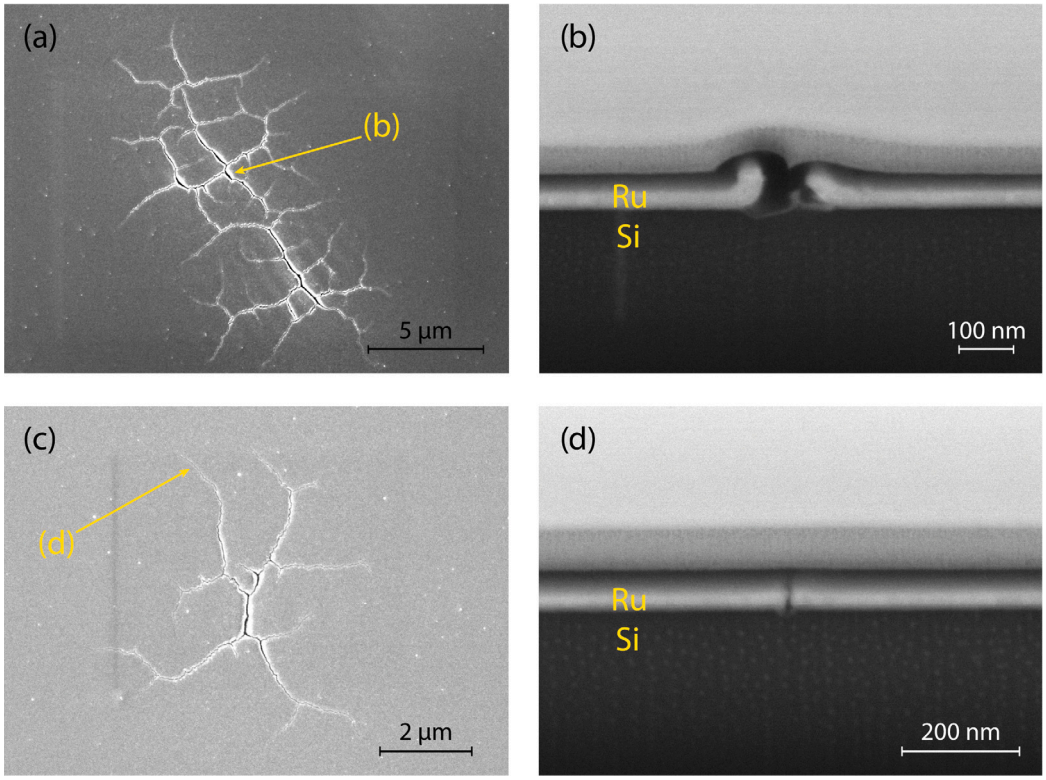

Fig. 6. (a) SEM image of a separate crack spot found at irradiated line 4, see Fig. 5(a). Yellow line indicates intense crack which depth was measured by FIB-SEM technique. (b) FIB-SEM image of the crack. The crack depth is equal to the entire film thickness. (c) SEM image similar to (a), but for a smaller crack spot. Yellow line indicates the edge of the crack characterized by FIB-SEM. (d) FIB-SEM image of the crack edge. The crack formation along the entire film thickness can be seen.

The heat source $S(t, z)$ is a product of a temporal Gaussian pulse and in-depth absorbed energy profile as follows:

$$S(t,z) = F\sqrt{\frac{4\ln 2}{\pi\tau_p^2}}e^{-4\ln 2(t/\tau_p)^2}A(z) \quad (3)$$

Here F is an incident fluence, τ_p is a pulse duration, and $A(z)$ is an absorbed energy profile. For bulk materials and films much thicker than the photons absorption length, $A(z)$ can be described by the Lambert–Beer absorption law. However, in the case of multilayer structures and thin films with the thickness comparable to the absorption length of photons, Lambert–Beer law breaks down (see Fig. 4). To account for the deviations of the absorption profile from the Lambert–Beer's law in the heat source, in our code we implemented the matrix algorithm (transfer-matrix approach) for the fields calculation [37].

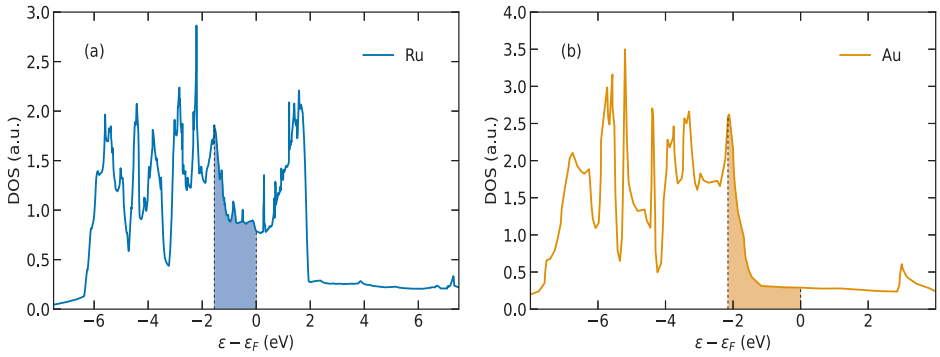

Fig. 7. (a) DOS of Ru taken from [40] and (b) Au from [43]. Blue fill in Ru DOS represents energy states allowing optical transitions for photons with energies $\hbar\omega = 1.55$ eV, orange fill in Au DOS — photons with energies equal to d-band transition threshold.

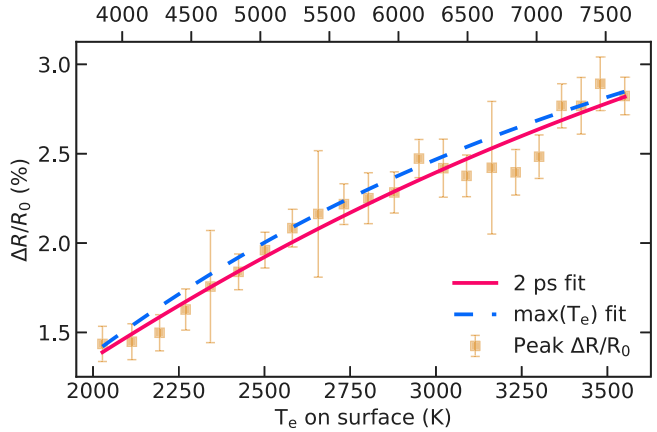

Fig. 8. Peak reflectance change $\Delta R/R_0$ as a function of electron temperature T_e (orange markers). Red line represents fitting by Fermi smearing function (1) for T_e at 2 ps, and blue dashed line is the same for max T_e value. The ticks on the lower horizontal axis indicate surface temperature values at 2 ps. For the upper axis, ticks correspond to the maximal values of electron temperature.

4.2. Fermi smearing mechanism in Ru

To relate experimentally measured change of thermoreflectance signal $\Delta R(t)/R_0$ and TTM-calculated temperatures $T_e(t)$, $T_l(t)$, one needs to know how optical constants depend on temperatures in two-temperature regime. T_l-dependence of optical properties is often neglected as far as heating of lattice subsystem does not cause any significant changes in electronic structure. In this work, we assume that the transient optical response of the electron system in Ru can be described in terms of the electron temperature T_e, same as in other transition metals [35,44]. However, finding an approximate form of T_e-dependence of Ru optical constants is a challenging task. Due to the complexity of Ru band structure near the Fermi level, a simple but widely accepted Drude model would not provide reliable results, whereas accurate DFT-based optical constants would require a set of computationally heavy calculations. Nevertheless, some qualitative information about optical response in Ru can be obtained if one recognizes a similarity in band structures of Ru and gold in the vicinity of the Fermi level.

We noticed that the electron density of states (DOS) of Ru (Fig. 7(a)) has a pseudo-gap near the Fermi level ranging from −1.5 to 1 eV, similarly to the gap between the majority of the d-band and the Fermi level in gold (Fig. 7(b)). As was pointed out in [45], for photon energies within this pseudo-gap area, the interband contribution to the optical transitions is weak, and at a qualitative level, a temperature dependence of the reflectance change in Ru may be explained via the Fermi smearing mechanism like in noble metals.

The Fermi smearing mechanism assumes that the change of reflectance is proportional to the change of Fermi distribution with increasing electron temperature, Eq. (4) [28,29].

$$\frac{\Delta R(\hbar\omega, T_e)}{R_0} \sim f(\hbar\omega, T_e) - f(\hbar\omega, T_0), \tag{4}$$

$$f(\hbar\omega, T_e) = \frac{1}{\exp\left(\frac{\hbar\omega + \Delta\varepsilon}{k_B T_e}\right) + 1}. \tag{5}$$

Here $\hbar\omega$ is the energy of incident photons equal to 1.55 eV, $\Delta\varepsilon = \varepsilon - \varepsilon_F$ is the difference between the energy level from which an electron is excited and the Fermi level of Ru, T_e and T_0 are the elevated and the initial electron temperatures, respectively. In our case, $\Delta\varepsilon$ is a priory unknown free parameter assumed to be constant for all temperatures, so ε has a meaning of an averaged energy level participating in optical transition.

The Fermi smearing mechanism works in the regime when the photon energy is close to the interband transition energy $\Delta\varepsilon$, which in the case of Ru we attribute to the lower boundary of the pseudo-gap. If we have fixed value $\hbar\omega = 1.55$ eV and variable parameter $\Delta\varepsilon$, we can try to fit temperature-dependent reflectance points by Eq. (4) with respect to $\Delta\varepsilon$. Then comparing the fitted value with the lower pseudo-gap boundary taken from Ru DOS will allow us to estimate to what extent the Fermi smearing is valid in Ru.

The T_e-dependence of the peak reflectance changes in Ru (Fig. 3) can be taken from the TTM model (Eq. (2)) with given incident fluence. For every fluence point, we got two electron temperature values: one is the highest surface temperature reached, and the other value is the temperature at ~2 ps after the laser pulse. The first value corresponds to an assumption that the peak change of reflectance corresponds to the maximal heating of the electronic system, and the second value assumes that the peak reflectance change corresponds to the process of electron-lattice equilibration. The result of fitting for 37 nm Ru film is shown in Fig. 8.

The fitted averaged energy level $\Delta\varepsilon$ is −1.20 eV for T_e at 2 ps. This value is close to the expected −1.5 eV, and thus indicates the validity of the Fermi smearing explanation of the electron temperature dependence of Ru optical properties. For the max T_e, the $\Delta\varepsilon$ value is −0.97 eV, which is far from the lower boundary of the pseudo-gap. This deviation confirms our suggestion to attribute the peak reflectance to the electron-lattice equilibration (reaching maximal lattice temperature, see Fig. 2(b)). Similar results were obtained for other Ru thicknesses. Nevertheless, the applicability of the Fermi smearing mechanism to Ru seems to be limited since the interband contribution to optical transitions is weak but non-vanishing. A more accurate quantitative explanation requires first-principles simulations of Ru in a similar manner to the work [45] and may be provided in our future works.

4.3. Damage threshold in Ru

In this section, we investigate the thickness-dependent damage thresholds. Having the SEM images (similar to Fig. 5) for all of the samples, we extract thickness-dependent data by attributing the onset of damage to surface cracking. To elaborate on the mechanism of damage we start our analysis with the calculations of the laser-induced melting thresholds.

We provide the calculation of melting thresholds in Ru irradiated by fs laser using two approaches. The first is a series of the TTM simulations (Section 4.1) for the different Ru thicknesses. The second is the two-temperature — molecular dynamics (TTM-MD) simulations for 75, 100 and 120 nm Ru films. We consider large thicknesses to avoid the effects of multiple reflections of light at the interfaces on the absorption profile and, hence, the necessity to include Si substrate into simulations. The TTM-MD simulations were based on the in-house MD code with the highly adaptive load balancing algorithm [46,47] allowing to simulate very large systems with a highly non-uniform mass distribution. In both performed approaches, the melting threshold was determined as fluence at which a surface layer of ~1 nm becomes liquid. We trace a modified centrosymmetric parameter C_s [48] averaged for atoms within the surface layer. It is known that the perfect hcp crystal has $C_s = 3$, whereas melting happens when C_s drops below 2.5, which is assumed to be a threshold for disordered atom configurations in a liquid phase. In the TTM simulations a layer is considered to be liquid when its lattice temperature overcomes the equilibrium melting temperature $T_l > T_m$, $T_m = 2607$ K. The results of the simulations and their comparison with the SEM-thresholds are shown in Fig. 9.

The discrepancy between thresholds taken from SEM and the fluences at which the pump-probe signal starts to increase (dR/dt) indicates that the pump-probe signal stays stable under minor surface changes such as cracks formation. Meanwhile, a factor two difference between experimentally determined thresholds and theoretically predicted melting thresholds most likely indicates that cracking occurs at lower fluences than melting. We suppose that one of the possible origins of cracking can be fast lateral expansion of a film during laser-induced heating followed by slow cooling due to dissipation of heat from the Ru film into the Si substrate. This leads to a generation of thermo-mechanical stresses accumulating on defects (e.g., grain boundaries or pores). When the stress amplitude reaches critical value, stress tears a film apart forming a crack propagating along the boundaries of defects. Our assumption is confirmed by the results of focused ion beam — scanning electron microscopy (FIB-SEM) analysis shown in Fig. 6. FIB-SEM allows to estimate the cracks depth. As one can see in Fig. 6(b) and (d), the entire Ru film is torn along the crack path. Most likely, it means that the centers of crack nucleation are not concentrated near film surface but most likely are uniformly distributed in the film.

Additional stresses in a film are generated due to the rotation of the sample. Their contribution can be estimated according to Eq. (55) from [49] for the radial and angular stress tensor components:

$$\sigma_r = \frac{3+\nu}{8}\rho\omega^2(R^2 - r^2),$$
$$\sigma_\theta = \frac{3+\nu}{8}\rho\omega^2 R^2 - \frac{1+3\nu}{8}\rho\omega^2 r^2$$

Here ν is the Poisson ratio of the material, ρ is the material density, ω is an angular velocity, R is the disk radius and r is a considered distance from the center of the disk. Using known parameters for solid Ru $\nu = 0.3$ and $\rho = 12.4\ \mathrm{g/cm^3}$, having $R = 3.8$ cm and typical position of the trace $r = 2$ cm, we get an estimation for additional stress $\sigma_r \approx \sigma_\theta \approx 2$ MPa. These values are at least three orders of magnitude lower than the tensile strength of hot Ru being 5–20 GPa depending on temperature and phase [16]. Thus, their influence on the formation of cracks seems to be negligible.

Albeit the theoretically predicted and experimentally observed thickness-dependent thresholds seem to attribute to different damaging mechanisms, they follow a common trend. Thresholds increase together with an increasing thickness of a film until some critical value around 75 nm after which they saturate. This critical thickness is associated with change of absorption from thin-film regime to bulk described by Lambert–Beer's law.

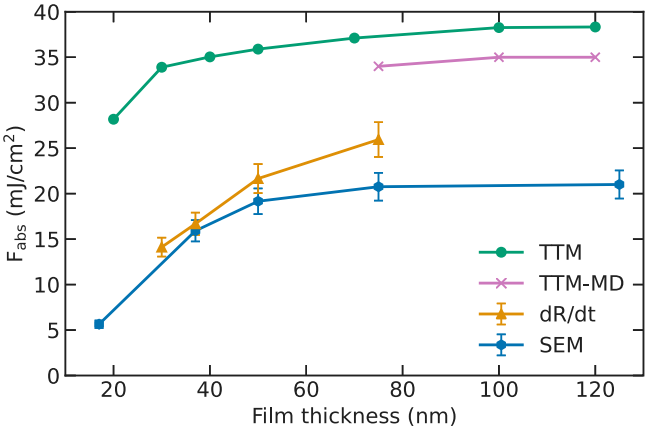

Fig. 9. Thickness-dependent threshold fluences of Ru films. Blue hexagons are values corresponding to the onset of the SEM-observed cracks, orange triangles correspond to the fluences at which pump-probe curves exhibit increase at long timescales (Table 1), green circles are the surface melting thresholds provided by the TTM simulations, and purple crosses are the thresholds taken from the TTM-MD simulations of thick Ru films.

Higher threshold values in the TTM than in the TTM-MD can be explained by the absence of the real surface in the TTM. The latent heat of fusion used in the TTM is taken for the bulk material, and thus does not reproduce the properties of the surface. In contrary, molecular dynamics natively takes into account the weaker bonding of surface atoms and thus describes the process of surface melting in a more natural way. It uses the EAM potential constructed specifically for Ru under intense ultrafast laser excitation and successfully applied to describe laser-induced ablation [16]. The melting temperature predicted by this potential is 2787 K, which is 7% higher than the experimental value being 2607 K and used in the TTM analysis. This leads to a few percent higher threshold values than one would expect from the experiment, but does not have a major impact on the obtained results.

5. Conclusion

We presented measurements of transient pump-probe thermoreflectance in Ru thin films as a function of incident fluence and Ru layer thickness in near-threshold regime. We applied rotational scheme to reduce heat accumulation in a target. An analysis of the measured thermoreflectance signal allowed us to extract information about behavior of hot electrons. However, we could not directly correlate the behavior of thermoreflectance curve to the threshold of irreversible changes in thin Ru films.

The results of hot electrons analysis indicated similarity of electron system response to laser irradiation for noble metals with fully occupied d-bands and Ru with half-filled d-band. We attributed this result to the presence of a pseudo-gap in Ru DOS around the energy of incident photons. Inside this pseudo-gap, interband transitions are weak, and Ru response may be qualitatively described via Fermi smearing mechanism. A similar effect is expected for other metals with pseudo-gap in d-band (e.g. Cr, W) and may be a scope for a dedicated research.

We demonstrated occurrence of three well-separated stages of surface changes during ultrafast laser heating of Ru film: darkening of an irradiation line, surface cracking and grooves formation. Our *post mortem* surface analysis associated appearance of the dark regions with increasing oxidation of the surface or growth of carbon layer.

We compared the cracks formation threshold to the two-temperature and molecular dynamics simulations of the melting

threshold. We found that the crack formation threshold is two times lower than theoretical predictions for single-shot melting threshold. This led us to the conclusion that the basic mechanism of cracking is formation of heat-induced stresses in a thin film leading to film tearing. Our results may serve as the upper limit of operational conditions for optic devices based on Ru thin films.

CRediT authorship contribution statement

Fedor Akhmetov: Writing – review & editing, Writing – original draft, Visualization, Software, Methodology, Investigation, Formal analysis, Data curation. **Igor Milov:** Writing – review & editing, Writing – original draft, Supervision, Project administration, Methodology, Investigation, Formal analysis, Conceptualization. **Sergey Semin:** Writing – review & editing, Validation, Methodology, Investigation, Formal analysis. **Fabio Formisano:** Writing – review & editing, Methodology, Investigation. **Nikita Medvedev:** Writing – review & editing. **Jacobus M. Sturm:** Writing – review & editing, Investigation. **Vasily V. Zhakhovsky:** Writing – review & editing, Software. **Igor A. Makhotkin:** Writing – review & editing, Supervision, Project administration, Conceptualization. **Alexey Kimel:** Resources, Project administration, Conceptualization. **Marcelo Ackermann:** Writing – review & editing, Supervision, Resources, Project administration, Funding acquisition.

Declaration of competing interest

The authors declare that they have no known competing financial interests or personal relationships that could have appeared to influence the work reported in this paper.

Data availability

Data will be made available on request

Acknowledgments

FA is grateful to H. van der Velde for fruitful discussions and technical assistance. AK and SS are grateful to C. Berkhout and A. Toonen for technical support.

FA, IMi, JS, IMa and MA acknowledge the Industrial Partnership Program 'X-tools', project number 741.018.301, funded by the Netherlands Organization for Scientific Research, ASML, Carl Zeiss SMT, and Malvern Panalytical.

For XTANT calculations, computational resources were supplied by the project "e-Infrastruktura CZ" (e-INFRA LM2018140) provided within the program Projects of Large Research, Development and Innovations Infra-structures. NM gratefully acknowledges financial support from the Czech Ministry of Education, Youth and Sports (Grants No.LM2018114, LTT17015 and No. EF16_013/0001552).

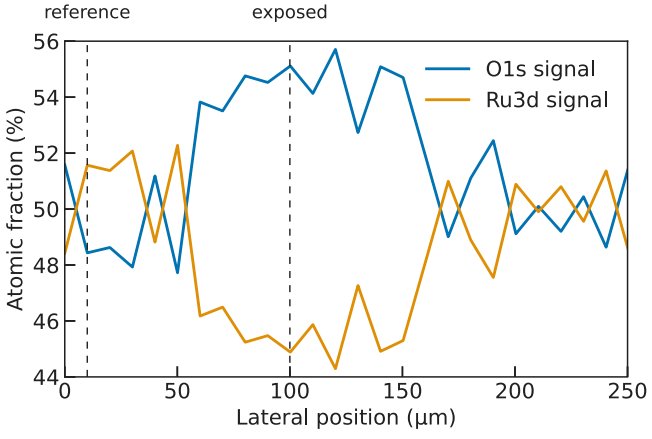

Fig. A.1. XPS O and Ru signals along a line scan perpendicular to the optically irradiated line on the sample. The vertical dashed lines 'reference' and 'exposed' indicate the positions where angle-resolved XPS measurements were performed for a reference point (outside the exposed area) and the exposed area.

Appendix A. XPS analysis

A.1. Experimental details

X-ray Photoelectron Spectroscopy (XPS) and Auger Electron Spectroscopy (AES) were performed with a Thermo Scientific Theta Probe instrument at a base pressure below 10^{-9} mbar. This instrument is equipped with a field emission gun for secondary electron imaging, which can be used to obtain AES spectra at a specific spot in a secondary electron microscopy image. AES was initially used to confirm that a higher oxygen concentration could be found in the optically exposed area. After this, XPS was used for more precise quantification of the Ru oxidation.

Monochromatic Al-Kα radiation was used for XPS analysis with an X-ray spot of 20 μm. The instrument collects photoelectrons in a range of ±30° around an average take-off angle of 53° with respect to the surface normal and can measure either angle-integrated or in parallel angle-resolved mode (AR-XPS). The binding energy scale of the

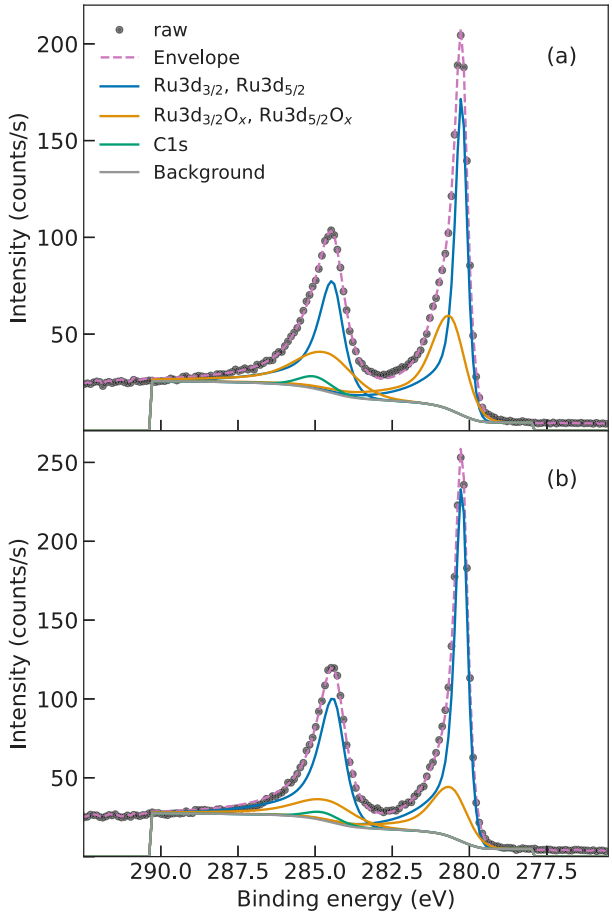

Fig. A.2. Ru3d XPS spectra of the optically exposed area (a) and the reference spot (b). Points indicate the measured signal, blue line — the fitted Ru metal doublet, orange line — the fitted RuO_x doublet and the green line — the fitted C1s signal. Gray line indicates the Shirley background, and lilac dashed line — envelope signal (sum of background and fitted peaks).

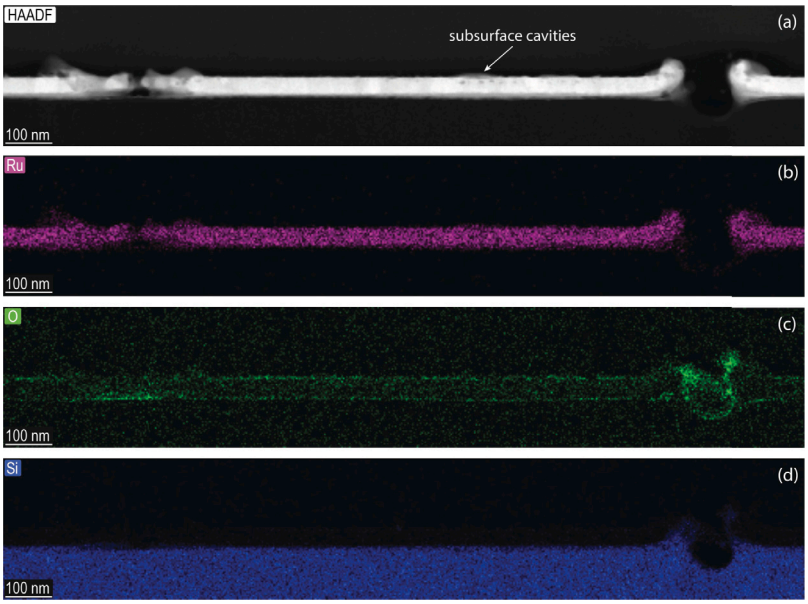

Fig. B.1. TEM-HAADF image of a lamella taken from laser-induced damage region (a) with EDX maps for Ru (b), O (c) and Si (c).

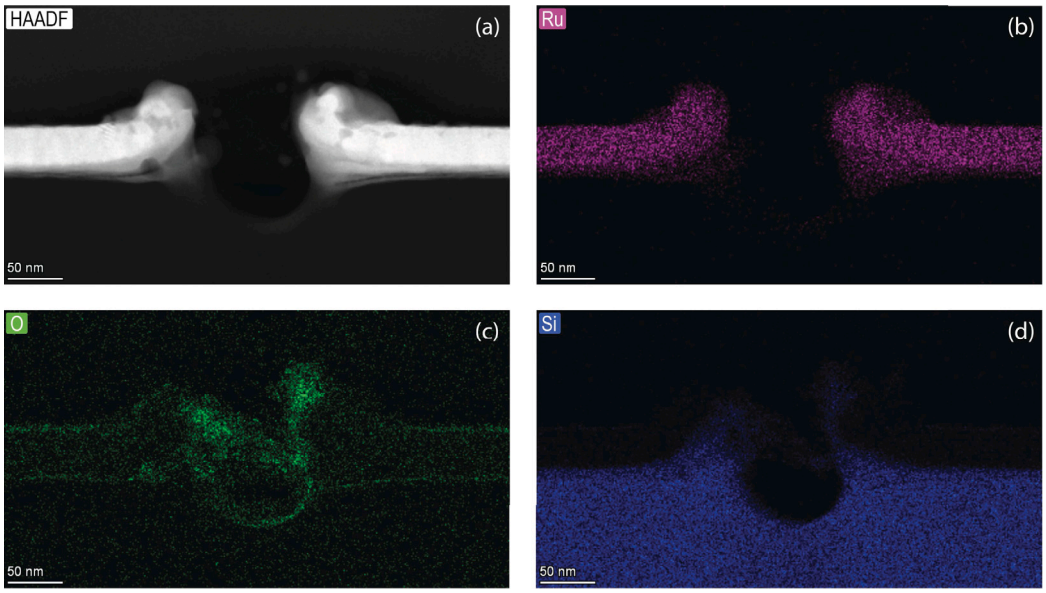

Fig. B.2. TEM-HAADF image of the crack region (a) with EDX maps for Ru (b), O (c) and Si (d).

instrument is calibrated based on reference measurements on sputter cleaned Au, Ag, and Cu foils, such that the binding energy of $Au4f_{7/2}$ is 84.0 eV, that of $Ag3d_{5/2}$ is 368.2 eV, and that of $Cu2p_{3/2}$ is 932.6 eV [50]. To ensure reliable XPS analysis, charge referencing is generally necessary to accurately align the energy scale [51,52]. However, in our specific case, the metallic Ru3d peak position is reproducible from sample to sample within 0.1 eV margin. We explain it by the good electrical conductivity of native ruthenium oxide [53,54] that preserves the charge neutrality of the sample surface. Therefore, we did not apply further referencing to the binding energy scale for this particular sample.

The center of the exposed (circular) line was found by performing an XPS line scan measurement across the exposed line with a step size of 10 μm, measuring the O1s and Ru3d signals. After this, the oxide thickness was determined by AR-XPS measurements at the spot with highest oxygen concentration and a reference point away from the spot with elevated oxygen concentration. The oxide thicknesses were calculated with the overlayer thickness calculator in the Thermo Scientific Avantage software, based on effective attenuation lengths according to the method of Cumpson and Seah [55]. All measurements were carried out without sample pre-treatment and without charge neutralization

A.2. Results

As described in Section 3.2, AES was initially used for determination of the difference in oxygen signal between the optically exposed circular ring and reference spots away from the exposed area. In order to better quantify the difference in oxidation, XPS measurements were performed. Fig. A.1 shows results of an XPS line scan across a line perpendicular to the circumference of the optically exposed circular ring. The O1s and Ru3d peak areas are quantified in terms of atomic % (neglecting the contribution of C1s, which is difficult to separate from the Ru3d signal). The XPS results show a slightly elevated O signal over

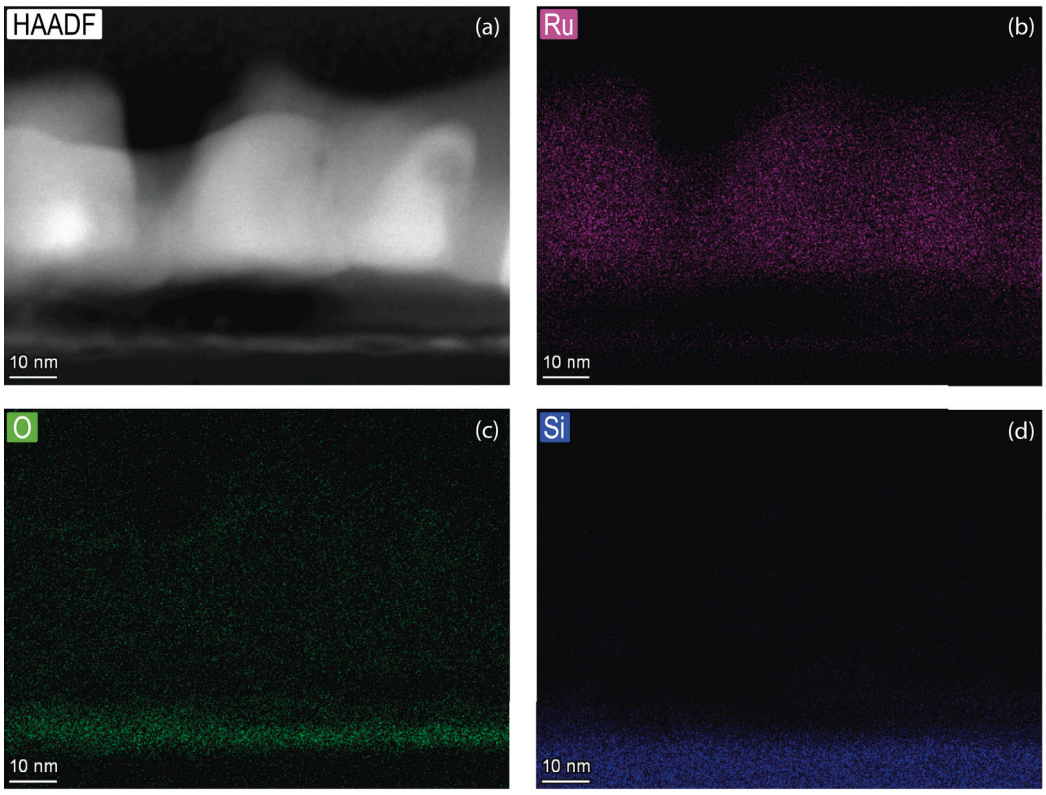

Fig. B.3. TEM-HAADF image of the partially stable film (a) with EDX maps for Ru (b), O (c) and Si (c).

a width of about 100 μm. In order to express the change in oxidation as oxide thickness, angle-resolved XPS measurements were performed on a reference spot (outside the exposed area) and on the exposed area, as depicted by the dashed lines in Fig. A.1.

Fig. A.2 shows the Ru3d spectra (for a photoelectron take-off angle of 34°) of the exposed (a) and reference (b) spots. Based on a separate reference measurement on sputter cleaned Ru, the spectra have been fitted with Ru3d doublets for Ru metal, Ru oxide and a peak for C1s, which overlaps with the $Ru3d_{3/2}$ peak. The increased oxidation in the exposed spot corresponds to a higher ratio of the RuO_x peak vs. Ru metal. Angle-resolved measurements of this ratio were analyzed to express the Ru oxidation as thickness of a RuO_2 film on Ru (assuming bulk densities). This yields RuO_2 thicknesses of 0.8 ± 0.2 nm and 1.2 ± 0.2 nm on the reference and exposed spots, respectively.

Appendix B. TEM-EDX analysis of damaged area

To support the results of the XPS analysis, the transmission electron microscopy (TEM)/energy-dispersive X-ray (EDX) mapping was also made. For this study, we chose a spot on line 3 (see Fig. 5(a)) because it consists of both areas of severe damage with cracks and areas of surface darkening, making it a suitable location to analyze both types of damage. Fig. B.1 shows an overview high-angle annular dark-field (HAADF) TEM image with two well-defined cracks and the corresponding element-specific EDX maps. Interestingly, a series of small subsurface cavities is observed, resembling frozen cavities simulated with MD method in EUV-irradiated Ru film (see Fig. 3(a) in [16]). Fig. B.1(c) shows the areas of high oxygen concentration in damaged regions (cracks) as well as on Ru surface and Ru-SiO_x/Si interface. Small amount of oxygen is present in the region between the two cracks inside Ru layer due to lamella oxidation during transportation to TEM. This type of oxidation is unavoidable.

Fig. B.2 shows zoomed-in TEM images of cracked area. According to Fig. B.2(c), oxygen content increases significantly only on crack boundaries and inside a crack. We relate this to transiently increased temperature due to laser irradiation and increased amount of Ru surface after crack formation.

Moving further from the center of laser spot (to the left from the region shown on Fig. B.1) we found a region which is similar to the left crack on Fig. B.1(a). In this region, the film is also detached from the substrate but remains closed. The particular importance of this region is the well-resolved image of separate Ru crystallites with pronounced boundaries between them, see Fig. B.3. We did not observe accumulation of oxygen on the grain boundaries as shown in Fig. B.3(c). This finding supports our conclusion that the concentration of oxygen inside a film is very low even after high level of irradiation and is not likely responsible for the character of observed damage.

Appendix C. Supplementary data

Supplementary material related to this article can be found online at https://doi.org/10.1016/j.vacuum.2023.112045.

References

[1] J. Bonse, J. Krüger, S. Höhm, A. Rosenfeld, Femtosecond laser-induced periodic surface structures, J. Laser Appl. 24 (4) (2012) 042006, http://dx.doi.org/10.2351/1.4712658, URL http://lia.scitation.org/doi/10.2351/1.4712658.

[2] M. Murakami, B. Liu, Z. Hu, Z. Liu, Y. Uehara, Y. Che, Burst-mode femtosecond pulsed laser deposition for control of thin film morphology and material ablation, Appl. Phys. Express 2 (4) (2009) 0425011–0425013, http://dx.doi.org/10.1143/APEX.2.042501.

[3] W. Han, L. Jiang, X. Li, Q. Wang, S. Wang, J. Hu, Y. Lu, Controllable plasmonic nanostructures induced by dual-wavelength femtosecond laser irradiation, Sci. Rep. 7 (1) (2017) 1–11, http://dx.doi.org/10.1038/s41598-017-16374-6.

[4] D. Zhang, B. Gökce, S. Barcikowski, Laser synthesis and processing of colloids: Fundamentals and applications, Chem. Rev. 117 (5) (2017) 3990–4103, http://dx.doi.org/10.1021/acs.chemrev.6b00468.

[5] Q. Yang, Z. Cai, Y. Wang, H. Huang, Y. Wu, Controllable crystallization of Ge2Sb2Te5 phase-change memory thin films driven by multiple femtosecond laser pulses, Mater. Sci. Eng. B 193 (C) (2015) 189–197, http://dx.doi.org/10.1016/j.mseb.2014.12.017.

[6] S. Edward, H. Zhang, S. Witte, P.C.M. Planken, Laser-induced ultrasonics for detection of low-amplitude grating through metal layers with finite roughness, Opt. Express 28 (16) (2020) 23374, http://dx.doi.org/10.1364/oe.398134.

[7] L. Zhao, C. Zhao, C. Xia, Z. Zhang, T. Wu, H. Xia, Nanometer precision time-stretch femtosecond laser metrology using phase delay retrieval, J. Lightwave Technol. 39 (15) (2021) 5156–5162, http://dx.doi.org/10.1109/JLT.2021.3079127.

[8] J.S. Oh, S.-W. Kim, Femtosecond laser pulses for surface-profile metrology, Opt. Lett. 30 (19) (2005) 2650, http://dx.doi.org/10.1364/ol.30.002650.

[9] H. Over, Surface chemistry of ruthenium dioxide in heterogeneous catalysis and electrocatalysis: From fundamental to applied research, Chem. Rev. 112 (6) (2012) 3356–3426, http://dx.doi.org/10.1021/cr200247n.

[10] D.W. Goodman, C.H. Peden, M.S. Chen, CO oxidation on ruthenium: The nature of the active catalytic surface, Surf. Sci. 601 (19) (2007) 18–20, http://dx.doi.org/10.1016/j.susc.2007.08.003.

[11] M.R. Axet, K. Philippot, Catalysis with colloidal ruthenium nanoparticles, Chem. Rev. 120 (2) (2020) 1085–1145, http://dx.doi.org/10.1021/acs.chemrev.9b00434.

[12] S. Bajt, N.V. Edwards, T.E. Madey, Properties of ultrathin films appropriate for optics capping layers exposed to high energy photon irradiation, Surf. Sci. Rep. 63 (2) (2008) 73–99, http://dx.doi.org/10.1016/j.surfrep.2007.09.001.

[13] A. Aquila, R. Sobierajski, C. Ozkan, V. Hájková, T. Burian, J. Chalupský, L. Juha, M. Störmer, S. Bajt, M.T. Klepka, P. Dłużewski, K. Morawiec, H. Ohashi, T. Koyama, K. Tono, Y. Inubushi, M. Yabashi, H. Sinn, T. Tschentscher, a.P. Mancuso, J. Gaudin, Fluence thresholds for grazing incidence hard X-ray mirrors, Appl. Phys. Lett. 106 (24) (2015) 241905, http://dx.doi.org/10.1063/1.4922380.

[14] I. Milov, I.A. Makhotkin, R. Sobierajski, N. Medvedev, V. Lipp, J. Chalupský, J.M. Sturm, K. Tiedtke, G. de Vries, M. Störmer, F. Siewert, R. van de Kruijs, E. Louis, I. Jacyna, M. Jurek, L. Juha, V. Hájková, V. Vozda, T. Burian, K. Saksl, B. Faatz, B. Keitel, E. Plönjes, S. Schreiber, S. Toleikis, R. Loch, M. Hermann, S. Strobel, H.-K. Nienhuys, G. Gwalt, T. Mey, H. Enkisch, F. Bijkerk, Mechanism of single-shot damage of Ru thin films irradiated by femtosecond extreme UV free-electron laser, Opt. Express 26 (15) (2018) 19665, http://dx.doi.org/10.1364/OE.26.019665.

[15] I. Milov, V. Lipp, D. Ilnitsky, N. Medvedev, K. Migdal, V. Zhakhovsky, V. Khokhlov, Y. Petrov, N. Inogamov, S. Semin, A. Kimel, B. Ziaja, I. Makhotkin, E. Louis, F. Bijkerk, Similarity in ruthenium damage induced by photons with different energies: From vis1. I. Milov, V. Lipp, D. Ilnitsky, N. Medvedev, K. Migdal, V. Zhakhovsky, V. Khokhlov, Y. Petrov, N. Inogamov, S. Semin, A. Kimel, B. Ziaja, I. A. Makhotkin, E. Louis, and, Appl. Surf. Sci. 501 (October 2019) (2020) 143973, http://dx.doi.org/10.1016/j.apsusc.2019.143973.

[16] I. Milov, V. Zhakhovsky, D. Ilnitsky, K. Migdal, V. Khokhlov, Y. Petrov, N. Inogamov, V. Lipp, N. Medvedev, B. Ziaja, V. Medvedev, I.A. Makhotkin, E. Louis, F. Bijkerk, Two-level ablation and damage morphology of Ru films under femtosecond extreme UV irradiation, Appl. Surf. Sci. 528 (February) (2020) 146952, http://dx.doi.org/10.1016/j.apsusc.2020.146952.

[17] I.A. Makhotkin, I. Milov, J. Chalupský, K. Tiedtke, H. Enkisch, G. de Vries, F. Scholze, F. Siewert, J.M. Sturm, K.V. Nikolaev, R.W.E. van de Kruijs, M.A. Smithers, H.A.G.M. van Wolferen, E.G. Keim, E. Louis, I. Jacyna, M. Jurek, D. Klinger, J.B. Pelka, L. Juha, V. Hájková, V. Vozda, T. Burian, K. Saksl, B. Faatz, B. Keitel, E. Plönjes, S. Schreiber, S. Toleikis, R. Loch, M. Hermann, S. Strobel, R. Donker, T. Mey, R. Sobierajski, Damage accumulation in thin ruthenium films induced by repetitive exposure to femtosecond XUV pulses below the single-shot ablation threshold, J. Opt. Soc. Amer. B 35 (11) (2018) 2799, http://dx.doi.org/10.1364/josab.35.002799.

[18] I.A. Makhotkin, R. Sobierajski, J. Chalupský, K. Tiedtke, G. de Vries, M. Störmer, F. Scholze, F. Siewert, R.W.E. van de Kruijs, I. Milov, E. Louis, I. Jacyna, M. Jurek, D. Klinger, L. Nittler, Y. Syryanyy, L. Juha, V. Hájková, V. Vozda, T. Burian, K. Saksl, B. Faatz, B. Keitel, E. Plönjes, S. Schreiber, S. Toleikis, R. Loch, M. Hermann, S. Strobel, H.-K. Nienhuys, G. Gwalt, T. Mey, H. Enkisch, Experimental study of EUV mirror radiation damage resistance under long-term free-electron laser exposures below the single-shot damage threshold, J. Synchrotron Radiat. 25 (1) (2018) 77–84, http://dx.doi.org/10.1107/S1600577517017362.

[19] K.R.P. Kafka, N. Talisa, G. Tempea, D.R. Austin, C. Neacsu, E.A. Chowdhury, Few-cycle pulse laser induced damage threshold determination of ultra-broadband optics, Opt. Express 24 (25) (2016) 28858, http://dx.doi.org/10.1364/oe.24.028858.

[20] T. Smausz, T. Csizmadia, C. Tápai, J. Kopniczky, A. Oszkó, M. Ehrhardt, P. Lorenz, K. Zimmer, A. Prager, B. Hopp, Study on the effect of ambient gas on nanostructure formation on metal surfaces during femtosecond laser ablation for fabrication of low-reflective surfaces, Appl. Surf. Sci. 389 (2016) 1113–1119, http://dx.doi.org/10.1016/j.apsusc.2016.08.026.

[21] P. Dominic, F. Bourquard, S. Reynaud, A. Weck, J.P. Colombier, F. Garrelie, On the insignificant role of the oxidation process on ultrafast high-spatial-frequency lipss formation on tungsten, Nanomaterials 11 (5) (2021) 1–10, http://dx.doi.org/10.3390/nano11051069.

[22] B.K. Nayak, M.C. Gupta, Self-organized micro/nano structures in metal surfaces by ultrafast laser irradiation, Opt. Lasers Eng. 48 (10) (2010) 940–949, http://dx.doi.org/10.1016/j.optlaseng.2010.04.010.

[23] W.S. Fann, R. Storz, H.W. Tom, J. Bokor, Electron thermalization in gold, Phys. Rev. B 46 (20) (1992) 13592–13595, http://dx.doi.org/10.1103/PhysRevB.46.13592.

[24] C.K. Sun, F. Vallée, L.H. Acioli, E.P. Ippen, J.G. Fujimoto, Femtosecond-tunable measurement of electron thermalization in gold, Phys. Rev. B 50 (20) (1994) 15337–15348, http://dx.doi.org/10.1103/PhysRevB.50.15337.

[25] S.-S. Wellershoff, J. Hohlfeld, J. Gudde, E. Matthias, The role of electron-phonon coupling in femtosecond laser damage of metals, Appl. Phys. A 69 (1) (1999) S99–S107, http://dx.doi.org/10.1007/s003399900305.

[26] B. Rethfeld, K. Sokolowski-Tinten, D. Von Der Linde, S.I. Anisimov, Timescales in the response of materials to femtosecond laser excitation, Appl. Phys. A 79 (4–6) (2004) 767–769, http://dx.doi.org/10.1007/s00339-004-2805-9.

[27] B. Rethfeld, D.S. Ivanov, M.E. Garcia, S.I. Anisimov, Modelling ultrafast laser ablation, J. Phys. D: Appl. Phys. 50 (19) (2017) http://dx.doi.org/10.1088/1361-6463/50/19/193001.

[28] W. Lynch, R. Rosei, Thermomodulation spectra of Al, Au, and Cu, Phys. Rev. B 5 (10) (1972) 3883–3894.

[29] R.W. Schoenlein, W.Z. Lin, J.G. Fujimoto, G.L. Eesley, Femtosecond studies of nonequilibrium electronic processes in metals, Phys. Rev. Lett. 58 (16) (1987) 1680–1683, http://dx.doi.org/10.1103/PhysRevLett.58.1680.

[30] G. de Haan, J. Hernandez-Rueda, P.C.M. Planken, Femtosecond time-resolved pump-probe measurements on percolating gold in the ablation regime, Opt. Express 28 (8) (2020) 12093, http://dx.doi.org/10.1364/oe.390509.

[31] O. Gunnarsson, P. Gies, W. Hanke, O.K. Andersen, Ab initio method for calculating response functions in transition metals, Phys. Rev. B 40 (18) (1989) 12140–12146, http://dx.doi.org/10.1103/PhysRevB.40.12140.

[32] I.G. Gurtubay, J.M. Pitarke, W. Ku, A.G. Eguiluz, B.C. Larson, J. Tischler, P. Zschack, K.D. Finkelstein, Electron-hole and plasmon excitations in 3d transition metals: Ab initio calculations and inelastic X-ray scattering measurements, Phys. Rev. B - Condens. Matter Mater. Phys. 72 (12) (2005) 1–11, http://dx.doi.org/10.1103/PhysRevB.72.125117.

[33] C. Ambrosch-Draxl, J.O. Sofo, Linear optical properties of solids within the full-potential linearized augmented planewave method, Comput. Phys. Comm. 175 (1) (2006) 1–14, http://dx.doi.org/10.1016/j.cpc.2006.03.005.

[34] M. Cazzaniga, L. Caramella, N. Manini, G. Onida, Ab initio intraband contributions to the optical properties of metals, Phys. Rev. B - Condens. Matter Mater. Phys. 82 (3) (2010) 1–7, http://dx.doi.org/10.1103/PhysRevB.82.035104.

[35] J. Hohlfeld, S.-S. Wellershoff, J. Güdde, U. Conrad, V. Jähnke, E. Matthias, Electron and lattice dynamics following optical excitation of metals, Chem. Phys. 251 (1–3) (2000) 237–258.

[36] R. Chartrand, Numerical differentiation of noisy, nonsmooth data, ISRN Appl. Math. 2011 (2011) 1–11, http://dx.doi.org/10.5402/2011/164564.

[37] UDCM-Group, AbsorptionTMM, 2019, URL https://github.com/udcm-su/AbsorptionTMM.

[38] S. Anisimov, B. Kapeliovich, T. Perel-man, Electron emission from metal surfaces exposed to ultrashort laser pulses, J. Exp. Theor. Phys. (1974).

[39] F. Akhmetov, N. Medvedev, I. Makhotkin, M. Ackermann, I. Milov, Effect of atomic-temperature dependence of the electron–phonon coupling in two-temperature model, Materials 15 (15) (2022) 5193, http://dx.doi.org/10.3390/ma15155193, URL https://www.mdpi.com/1996-1944/15/15/5193.

[40] Y. Petrov, K. Migdal, N. Inogamov, V. Khokhlov, D. Ilnitsky, I. Milov, N. Medvedev, V. Lipp, V. Zhakhovsky, Ruthenium under ultrafast laser excitation: Model and dataset for equation of state, conductivity, and electron-ion coupling, Data in Brief 28 (2020) 104980, http://dx.doi.org/10.1016/j.dib.2019.104980.

[41] S.P. Zhvavyi, G.D. Ivlev, Influence of the initial temperature of silicon on crystallization of a layer melted by nanosecond laser heating, J. Eng. Phys. Thermophys. 69 (5) (1997) 790–793.

[42] N.M. Bulgakova, R. Stoian, A. Rosenfeld, I.V. Hertel, W. Marine, E.E. Campbell, A general continuum approach to describe fast electronic transport in pulsed laser irradiated materials: The problem of Coulomb explosion, Appl. Phys. A 81 (2) (2005) 345–356, http://dx.doi.org/10.1007/s00339-005-3242-0.

[43] A. Blumenstein, E.S. Zijlstra, D.S. Ivanov, S.T. Weber, T. Zier, F. Kleinwort, B. Rethfeld, J. Ihlemann, P. Simon, M.E. Garcia, Transient optics of gold during laser irradiation: From first principles to experiment, Phys. Rev. B 101 (16) (2020) 1–9, http://dx.doi.org/10.1103/PhysRevB.101.165140.

[44] P.M. Norris, A.P. Caffrey, R.J. Stevens, J.M. Klopf, J.T. McLeskey, A.N. Smith, Femtosecond pump-probe nondestructive examination of materials (invited), Rev. Sci. Instrum. 74 (1 II) (2003) 400–406, http://dx.doi.org/10.1063/1.1517187.

[45] E. Bévillon, R. Stoian, J.P. Colombier, Nonequilibrium optical properties of transition metals upon ultrafast electron heating, J. Phys. Condens. Matter 30 (38) (2018) http://dx.doi.org/10.1088/1361-648X/aad8e5.

[46] V. Zhakhovskii, K. Nishihara, Y. Fukuda, S. Shimojo, T. Akiyama, S. Miyanaga, H. Sone, H. Kobayashi, E. Ito, Y. Seo, M. Tamura, Y. Ueshima, A new dynamical domain decomposition method for parallel molecular dynamics simulation, in: 2005 IEEE International Symposium on Cluster Computing and the Grid, Vol. 2, CCGrid 2005, 2005, pp. 848–854, http://dx.doi.org/10.1109/CCGRID.2005.1558650.

[47] M.S. Egorova, S.A. Dyachkov, A.N. Parshikov, V.V. Zhakhovsky, Parallel SPH modeling using dynamic domain decomposition and load balancing displacement of Voronoi subdomains, Comput. Phys. Comm. 234 (2019) 112–125, http://dx.doi.org/10.1016/j.cpc.2018.07.019.

[48] S. Murzov, S. Ashitkov, E. Struleva, P. Komarov, V. Zhakhovsky, V. Khokhlov, N. Inogamov, Elastoplastic and polymorphic transformations of iron at ultra-high strain rates in laser-driven shock waves, J. Appl. Phys. 130 (24) (2021) http://dx.doi.org/10.1063/5.0076869.

[49] S. Timoshenko, J.N. Goodier, Theory of Elasticity: By S. Timoshenko and JN Goodier, McGraw-Hill, 1951.

[50] M.P. Seah, Summary of ISO/TC 201 standard: VII ISO 15472 : 2001 - surface chemical analysis - X-ray photoelectron spectrometers - calibration of energy scales, Surf. Interface Anal. 31 (8) (2001) 721–723, http://dx.doi.org/10.1002/sia.1076.

[51] G. Greczynski, L. Hultman, Compromising science by ignorant instrument calibration—Need to revisit half a century of published XPS data, Angew. Chem. Int. Edn 59 (13) (2020) 5002–5006, http://dx.doi.org/10.1002/anie.201916000.

[52] G. Greczynski, L. Hultman, X-ray photoelectron spectroscopy: Towards reliable binding energy referencing, Prog. Mater. Sci. 107 (July 2019) (2020) 100591, http://dx.doi.org/10.1016/j.pmatsci.2019.100591.

[53] J. Riga, C. Tenret-Noël, J.J. Pireaux, R. Caudano, J.J. Verbist, Y. Gobillon, Electronic structure of rutile oxides TiO2, RuO2 and IrO2 studied by X-ray photoelectron spectroscopy, Phys. Scr. 16 (5–6) (1977) 351–354, http://dx.doi.org/10.1088/0031-8949/16/5-6/027.

[54] M.M. Steeves, Electronic Transport Properties of Ruthenium and Ruthenium Dioxide Thin Films (Ph.D. thesis), The University of Maine PP, United States – Maine, 2011, p. 159, URL https://digitalcommons.library.umaine.edu/etd/262, ProQuest Dissertations and Theses.

[55] P.J. Cumpson, M.P. Seah, Elastic scattering corrections in AES and XPS. II. Estimating attenuation lengths and conditions required for their valid use in overlayer/substrate experiments, Surf. Interface Anal. 25 (6) (1997) 430–446, http://dx.doi.org/10.1002/(SICI)1096-9918(199706)25:6<430::AID-SIA254>3.0.CO;2-7.